Journal of Applied Physics

RESEARCH ARTICLE | OCTOBER 09 2025

Role of neutron Bragg-edge spectroscopy in development of practical magnetic materials

Hiroaki Mamiya ; Noriki Terada ; Kosuke Hiroi ; Takenao Shinohara ; Hossein Sepehri-Amin

J. Appl. Phys. 138, 143904 (2025)
https://doi.org/10.1063/5.0285904

Journal of Applied Physics ARTICLE pubs.aip.org/aip/jap

Role of neutron Bragg-edge spectroscopy in development of practical magnetic materials

Cite as: J. Appl. Phys. **138**, 143904 (2025); doi: 10.1063/5.0285904
Submitted: 18 June 2025 · Accepted: 19 September 2025 ·
Published Online: 9 October 2025

Hiroaki Mamiya,[1,a)] Noriki Terada,[1] Kosuke Hiroi,[2] Takenao Shinohara,[2] and Hossein Sepehri-Amin[1]

AFFILIATIONS

[1]National Institute for Materials Science, Tsukuba 305-0047, Japan
[2]Japan Atomic Energy Agency, Tokai 319-1195, Japan

[a)]**Author to whom correspondence should be addressed:** mamiya.hiroaki@nims.go.jp

ABSTRACT

Neutron diffractometry plays a pivotal role in fundamental magnetism research, especially in determining magnetic structures. However, its application in practical magnetics was historically sparse due to the simplicity of ferromagnetic materials in conventional devices. Recent increase in utilization of materials with complex magnetic structures has introduced new challenges that necessitate advanced neutron techniques in applied magnetics. This study investigates the applicability of neutron Bragg-edge spectroscopy for developing practical magnetic materials, substantiating its effectiveness through experimental validations and theoretical analysis. We discuss the principles of Bragg-edge spectroscopy for magnetic materials and highlight enhanced experimental throughput using multisample transmission spectroscopy. The study provides insights into the *in situ* visualization of magnetic state distribution using Bragg-edge imaging, both post-assembly and during operational use. These results indicate that neutron Bragg-edge spectroscopy can address emerging needs in applied magnetics, offering significant advancements in the field.

I. INTRODUCTION

X-ray diffraction is indispensable for analyzing crystal structures, while neutron scattering excels in examining magnetic structures. Despite their critical roles, the application of these techniques in applied magnetics, particularly for practical materials, is relatively limited compared to their widespread use in the study of fundamental magnetism concerning condensed matter. For example, approximately one-quarter of the papers in *Physical Review B* that mention "magnetic" also reference "neutron." In contrast, the ratio was only approximately 1.7% of the papers in *IEEE Transactions on Magnetics*.[1] This discrepancy arises from the significant focus on ferromagnetic materials with uniformly aligned spins in practical applications during the 20th century. On the other hand, research in fundamental magnetism has progressively concentrated on more complex magnetic structures, primarily using neutron scattering. Consequently, the exploration of magnetic structures and excitations forms a significant part of neutron applications in fundamental magnetism. Highlighting this significance, at the 1994 International Conference on Neutron Scattering[2]—the year Professors Bertram N. Brockhouse and Clifford G. Shull were honored with the Nobel Prize for developing neutron scattering techniques—approximately one-third of the papers featured the term "magnetic" in their titles or abstracts. As a result, neutron technology has continuously evolved to meet the sophisticated demands of fundamental magnetism, which increasingly requires enhanced sensitivity and resolution. Today, neutron science stands at the forefront of large-scale scientific research, focusing on meticulously chosen samples to advance the fundamental understanding.

Since the late 20th century, the application of knowledge from fundamental magnetism has led to the increased use of materials with non-ferromagnetic structures, such as antiferromagnets, in applied magnetics. Notably, the antiferromagnet $HoCu_2$ has been utilized as a heat storage material,[3] enabling efficient cooling of Gifford–McMahon refrigerators to 4 K, which has ensured the widespread adoption of liquid helium-free MRI systems. Similarly, using the antiferromagnetic material IrMn as the pinning layer in spin valves has substantially enhanced the storage capacity of hard disk drives,[4] thereby contributing significantly to the IT revolution. These advancements using a non-uniform magnetic structure extend beyond microscale spin arrangements to mesoscale phases,

including the use of nanogranular recording media[5] and nanocomposite magnets.[6] At the macroscale, functionally graded magnetic materials[7] and multi-material components[8] are being developed, with magnetic properties engineered to vary within a single component. In the future, it is expected that practical magnetic materials will increasingly feature complex internal magnetic structures, moving away from a uniform magnetic state.

When leveraging complex internal magnetic structures, it is essential to assess these structures sequentially throughout every stage of material development, from optimization to assembly. To achieve this, the use of neutrons is indispensable at each stage. In the material development stage, a critical need exists for high-throughput evaluation methods to enable the optimization of compositions, structures, and processing parameters. Comprehensive assessments post-assembly or during operation are essential in the next implementation stage. Although current neutron diffraction facilities have evolved significantly in advancing the understanding of fundamental magnetic phenomena through high-accuracy/high-resolution measurements, it is unclear whether they can meet these emerging requirements. If challenges remain, alternative methodologies need to be explored.

In this study, we initially investigated the application of the increasingly recognized neutron transmission spectroscopy[9,10] to various magnetic materials, incorporating findings from experimental validations and theoretical analysis to determine the insights this method can provide. Subsequently, we determined the capacity of neutron transmission spectroscopy to address the new demands in the development of practical magnetic materials, focusing on throughput and *in situ* imaging. Based on the identified benefits and limitations of this spectroscopic method, we demonstrate its important role in advancing the development of next-generation magnetic materials.

II. EXPERIMENTAL

A single crystal of holmium, with a purity of 99.99%, was procured from Accumet Materials Co. The crystal was fashioned into plate-like shapes measuring approximately $1 \times 1 \times 0.5\ \mathrm{mm}^3$ and installed in a cryostat maintained at 4 K, devoid of any magnetic field. Ultra-fine-grained high-carbon steel containing 0.87 wt. % carbon was sourced from Tokushu Kinzoku Excel Co., Ltd. Twelve sheets of this steel were stacked and stored at room temperature without a magnetic field influence (this sample was previously utilized in studies reporting transmission spectra under a magnetic field of 0.4 MA/m[11]). A magnetic core made of non-oriented electrical steel was manufactured by Nippon Cut Core Trans Co., Ltd. This core was fabricated by winding sheets of Nippon Steel's Hi-Lite Core 35H360 (6 mm wide, 0.35 mm thick) to a total thickness of 10 mm, followed by stress-relief annealing at 800 °C. Since neutrons were irradiated from the side, the thickness along the transmission direction t_{actual} was 6 mm. A magnetomotive force within the core was generated using a permanent magnet ($10 \times 7 \times 5\ \mathrm{mm}^3$) integrated into a gap at the core's base, which was sourced from Niroku Seisakusho and exhibits a residual magnetic flux density of 1.2 T.

All transmission spectra were recorded as functions of the time-of-flight (ToF) of neutrons at beamline 22 (BL22) RADEN[12] at J-PARC. The neutron beam was polarized vertically using a magnetic mirror or antiparallelly through a spin flipper, as required prior to striking the sample. Detection of transmitted neutrons was conducted using a boron-coated gas electron multiplier for room temperature experiments, or a μPIC-based neutron imaging detector equipped with a boron converter for cryogenic temperature experiments.[13]

III. RESULTS AND DISCUSSION

A. Neutron transmission spectroscopy

It has been well established that when neutrons encounter an array of nuclei or magnetic moments with periodic structures,[14] denoted as $\boldsymbol{Q}_\tau$ and $\boldsymbol{Q}'_\tau$, respectively, Bragg's diffraction occurs if the scattering vector $\boldsymbol{q}$ is equal to $\boldsymbol{Q}_\tau$ or $\boldsymbol{Q}'_\tau$. The differential cross section, $d\sigma^{\mathrm{Bragg}}/d\Omega$, for unpolarized neutrons can be described as

$$\frac{d\sigma^{\mathrm{Bragg}}}{d\Omega} = N\frac{(2\pi)^3}{v_0}\sum_\tau \left[|F_{\mathrm{N}}(\boldsymbol{q})|^2\delta(\boldsymbol{q}-\boldsymbol{Q}_\tau) + |F_{\mathrm{M}}(\boldsymbol{q})|^2\delta(\boldsymbol{q}-\boldsymbol{Q}'_\tau)\right], \tag{1}$$

where N is the total number of unit cells; v_0 denotes the unit cell volume; and $F_{\mathrm{N}}(\boldsymbol{q})$ and $F_{\mathrm{M}}(\boldsymbol{q})$ are the crystal and magnetic structure factors, respectively. This principle forms the basis for neutron diffractometry for a crystal.[14] When diffraction occurs, the intensity of the transmitted beam decreases at the corresponding wavelength by a specific amount.[15,16] Consequently, dips (referred to as magnetic Bragg dips) are expected to appear in the transmission spectrum $Tr(\lambda)$ at λ, which satisfy the Laue condition $\boldsymbol{q} = \boldsymbol{Q}_\tau$.

As expected, we observed this type of dip in the transmission spectrum when measuring the wavelength dependence with a neutron detector positioned behind the sample,[17] as shown in Fig. 1(a). For instance, Fig. 1(b) displays the transmission spectrum for neutrons incident on the *c*-plane of a 0.5 mm thick pure holmium single crystal. At a temperature of 150 K, which is in the paramagnetic state, a pronounced dip appears at a wavelength corresponding to twice the (002) plane spacing of holmium in its hexagonal close-packed structure. This dip is due to backscatter diffraction from the (002) plane of the holmium crystal. Conversely, at a temperature of 30 K, below the Néel temperature of holmium at 132 K,[18] two additional dips, termed satellite dips, flank the original dip. These satellite dips suggest the formation of a magnetic structure characterized by a long periodicity that matches the distance between these satellites. Thus, similar to the conventional use of magnetic diffraction for determining magnetic structures, the observation of such "magnetic Bragg dips" provides significant insights into spin configurations in a single crystal.[17]

In the case of polycrystalline materials, these dips are unique to individual crystals within the sample. It is important to note that for any orientation of microcrystals, diffraction does not occur if the wavelength λ exceeds twice the interplanar spacing d_τ due to the Bragg condition: $2d_\tau \sin\theta = n\lambda$, where θ is the diffraction angle and n is an integer representing the order of diffraction. Consequently, several edge-like features, known as magnetic Bragg edges, manifest at $\lambda = 2d$ in the spectrum of a polycrystalline material. Figure 2(a) schematically depicts this relationship.

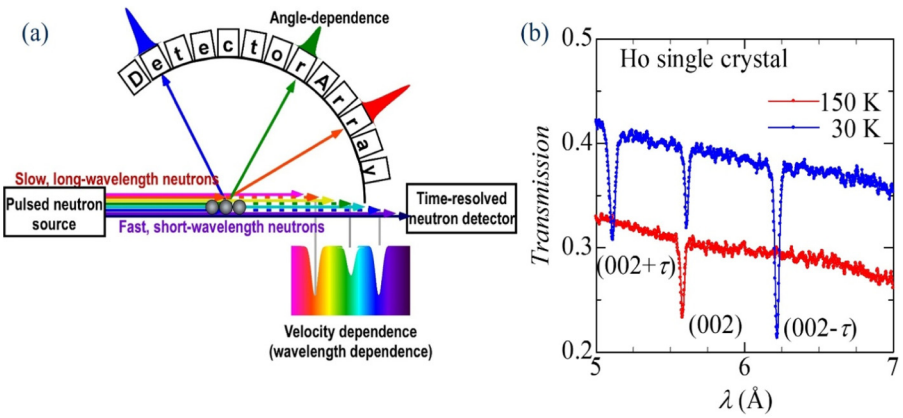

FIG. 1. Principle and typical results of neutron transmission spectroscopy for a single crystal. (a) Schematic demonstrating the principle of decreasing transmission at wavelengths where diffraction occurs and (b) transmission spectra for the Ho single crystal when unpolarized neutrons are incident on the c-plane. At 30 K, below the Néel temperature, two satellite dips caused by magnetic diffraction are evident in the spectra.

As diffraction varies from backscattering to forward scattering depending on the orientation distribution of microcrystals, the analysis of such spectra often employs the Rietveld method.[19] At this point, let us fully express the spectra using the following equation:[15]

$$Tr(\lambda) = \exp\left[-\sum_i \left(\sigma_i^{\text{Bragg}} + \sigma_i^{\text{TDS}} + \sigma_i^{\text{abs}}\right) n_i t_i\right], \tag{2}$$

where i denotes the ith phase of the multiphase material in multicomponent devices. The decay of neutron transmission is influenced by three critical cross sections: the elastic coherent Bragg diffraction cross section σ_i^{Bragg}, thermal diffuse scattering cross section σ_i^{TDS}, and absorption cross section σ_i^{abs}. Additionally, n_i and t_i represent the total number of unit cells in the unit volume and the effective thickness of the ith phase, respectively. Among these terms, σ_i^{Bragg} is of particular interest and can be written as follows:[14,19]

$$\sigma_i^{\text{Bragg}} = \frac{\lambda^2}{2v_0} \sum \left[|F_N(\boldsymbol{q})|^2 \delta(\boldsymbol{q} - \boldsymbol{Q}_\tau) + |F_M(\boldsymbol{q})|^2 \delta(\boldsymbol{q} - \boldsymbol{Q}'_\tau)\right] d_\tau P_\tau E_\tau, \tag{3}$$

where v_0 is the unit cell volume, P_τ is the preferred orientation factor, and E_τ is the extinction factor. Figure 2(b) displays the spectrum for the high-carbon steel plate, a typical example of a practical polycrystalline magnetic material, in a zero magnetic field. As anticipated, the transmission of unpolarized neutrons exhibits a significant decrease in the wavelength range below the backscattering wavelength for each set of lattice planes $\{hkl\}$. Upon closer inspection, the attenuation due to {200} diffraction is notably pronounced near $\theta = \pi/2$, while the attenuation due to {110} diffraction is most apparent around $\theta = \pi/3$. These patterns indicate that the (110) planes of most microcrystals were inclined away from the rolling surface, whereas the (200) planes tended to

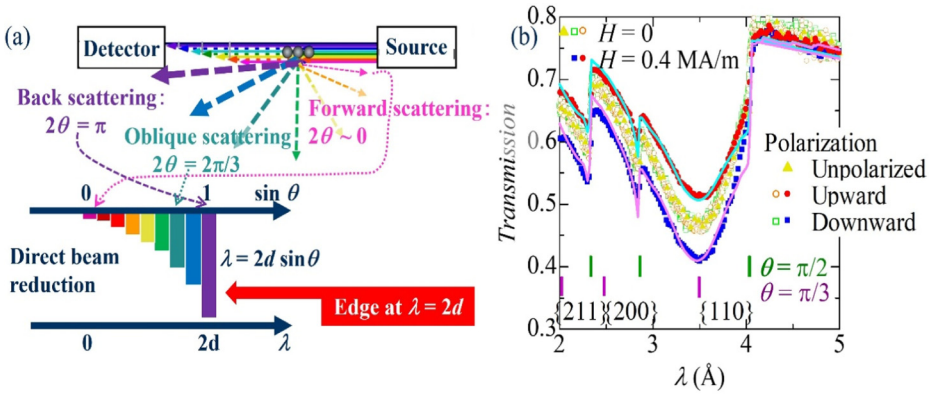

FIG. 2. Neutron transmission spectroscopy principles and typical results for polycrystalline materials. (a) Schematic showing diffraction and transmission through microcrystals with varying orientations of diffraction planes and (b) transmission spectra of a carbon steel plate for neutrons incident on the rolling face, displayed for both unpolarized and vertically polarized neutrons (data in the magnetic field were retrieved from Ref. 11). For context, the spectrum under the zero magnetic field is compared with results obtained in a magnetic field. The bars in the figure denote the wavelengths at which backward and oblique scattering occur for each diffraction plane.

align parallel to it. Further discussion of the incline has been carried out by applying a model function[11] for P_τ.

Let us now consider the details of the magnetic state that holds our interest. In ferromagnetic materials such as steel, where $\boldsymbol{Q}_\tau = \boldsymbol{Q}'_\tau$, no separate magnetic Bragg edge exists distinct from the edge due to nuclear scattering. For iron atoms, which possess magnetic moments of 2.2 bohr magnetons (μ_B), the magnitude of $|F_M(\boldsymbol{q})|^2$ is typically no more than 10% of $|F_N(\boldsymbol{q})|^2$ around $Q_\tau = 3$ Å^{-1} ($d_\tau = 2$ Å). This makes it challenging to discern the magnetic scattering cross section from spectra obtained using unpolarized neutrons. Consequently, neutron diffractometry often relies on polarized neutrons to reveal the magnetic structure of ferromagnetic materials. For neutrons polarized either upward or downward along the z-axis, the part inside the brackets in Eq. (1) can be reformulated as $[(F_N(\boldsymbol{Q}_\tau)\delta(\boldsymbol{q}-\boldsymbol{Q}_\tau) \mp F_M^{nsf}(\boldsymbol{Q}'_\tau)\delta(\boldsymbol{q}-\boldsymbol{Q}'_\tau))^2 + (F_M^{sf}(\boldsymbol{Q}'_\tau)\delta(\boldsymbol{q}-\boldsymbol{Q}'_\tau))^2]$ using magnetic structure factors for non-spin-flip and spin-flip scatterings,[20]

$$F_M^{nsf}(\boldsymbol{Q}'_\tau) = \sum_j o_j \left(r_m \frac{m_{\perp j}^z}{2\mu_B} f_j \right) \exp(i\boldsymbol{r}_j \cdot \boldsymbol{Q}'_\tau), \tag{4a}$$

$$F_M^{sf}(\boldsymbol{Q}'_\tau) = \sum_j o_j \left(-r_m \frac{m_{\perp j}^x - i m_{\perp j}^y}{2\mu_B} f_j \right) \exp(i\boldsymbol{r}_j \cdot \boldsymbol{Q}'_\tau), \tag{4b}$$

where r_m is the magnitude factor (5.39 fm); o_j is the site occupancy; $\boldsymbol{m}_{\perp j} = (m_{\perp j}^x, m_{\perp j}^y, m_{\perp j}^z)$; f_j represents the site occupancy; and the vector projection of the magnetic moment $\boldsymbol{m}_j$ of the jth atom on the plane perpendicular to $\boldsymbol{q}$ and the magnetic form factor of the jth atom, respectively. By employing polarized neutrons, we can detect relatively subtle changes in $F_M(\boldsymbol{Q}_\tau)$ by analyzing the more substantial cross terms of $F_M(\boldsymbol{Q}_\tau)\cdot F_M^{nsf}(\boldsymbol{Q}_\tau')$.

Figure 2(b) also depicts the previously reported transmission spectra obtained for the same sample in the presence of a magnetic field ($H = 0.4$ MA/m) applied along the vertical axis. The spectra in Fig. 2(b) reveal a notable difference in transmission depending on the direction of neutron polarization when a magnetic field ($H = 0.4$ MA/m) is applied vertically. In contrast, no such difference is observed in the current result obtained in a zero magnetic field. This phenomenon suggests that the application of $\boldsymbol{H}$ aligns the magnetic moment $\boldsymbol{m}_{\perp j}$ of each iron atom parallel to $\boldsymbol{H}$, resulting in significant changes in transmission as σ_i^{Bragg} either decreases or increases due to the interaction $2F_M(\boldsymbol{Q}_\tau)\cdot F_M^{nsf}(\boldsymbol{Q}_\tau')$. More detailed magnetic information can be derived from these powder spectra using full pattern fitting with the model described by Eqs. (3) and (4).[19]

As discussed thus far, it is feasible, in principle, to conduct structural analysis using neutron transmission spectroscopy, similar to neutron diffractometry. However, each method has its own advantages and disadvantages. For example, in a randomly oriented powder composed of atoms with a magnetic moment of $1\,\mu_B$ arranged on a face-centered cubic lattice with a lattice constant of 0.35 nm, the magnetic backscattering cross section from the (111) plane can be calculated to be approximately 30 fm^2 per atom. For a sample thickness of 1 cm, this corresponds to about 3% of the incident neutrons being scattered. If 10 000 neutrons are incident on a 1 cm^2 sample surface, 9700 neutrons will be transmitted and detected by a zero-dimensional counter with a 1 cm^2 aperture, resulting in a signal-to-noise (S/N) ratio of approximately $\frac{300}{\sqrt{9700}} \sim 3$. In contrast, assuming a large area detector (10^3–10^4 cm^2) with solid angle coverage of 30% in a diffractometer, 100 neutrons would be detected, corresponding to an S/N ratio of approximately $\frac{100}{\sqrt{100}} \sim 10$. Thus, when the magnetic moment is relatively small, the signal-to-noise ratio is, in principle, more favorable for diffractometry than for transmission spectroscopy. Conversely, in cases where the background level per unit detection area is high, transmission spectroscopy may demonstrate superiority with respect to the signal-to-background ratio. In any case, the relative merits of these methods depend on the specific sample and experimental setup. Therefore, in Sec. III B, we further investigate the potential of transmission spectroscopy through specific measurement examples and assess its suitability for the development of practical magnetic materials, focusing on measurement throughput and comprehensive *in situ* imaging, as outlined in the Introduction.

B. Potential of neutron transmission spectroscopy

1. Multi-sample spectroscopy

During the material optimization stage, numerous samples are produced to refine their composition and processing conditions. High throughput is essential for efficiently evaluating these materials. In diffractometry, intensity measurements for each scattering angle are typically conducted on a single sample centered within the detector array. The measurement time per sample can be reduced by increasing either the intensity of the incident neutron beam or the area of the detectors. Furthermore, if sample exchanges are conducted swiftly, measurement throughput can be significantly improved, even though each sample is measured individually.[21–23] However, under specialized conditions tailored to practical environments, sample auto-changers are sometimes not usable. In such cases, the entire process—including installing a sample, preparing the experimental environment, conducting measurements, waiting for the sample's residual radioactivity to diminish and, subsequently, exchanging the sample—may require up to a full day for a single specimen. This duration is independent of the neutron source intensity. Consequently, studies involving the comparison of a large number of samples—such as investigations into the compositional dependence of multi-element doped systems or the effects of subtle process conditions—demand significant and valuable beamline time, making their implementation difficult.

How does neutron transmission spectroscopy perform in comparison? In this section, we consider the case in which a neutron beam with a small divergence angle is divided into multiple parallel beams by means of a mask with numerous apertures. These parallel beams travel rectilinearly and reach the detector directly without intersecting one another. By aligning the samples and detectors along parallel paths, it is possible to obtain their spectra separately. Figure 3 illustrates a conceptual diagram of an experiment conducted with holmium alloys, alongside the representative results obtained. While detailed descriptions are provided in the original publication,[24] this experiment successfully captured the spectra of 25 different

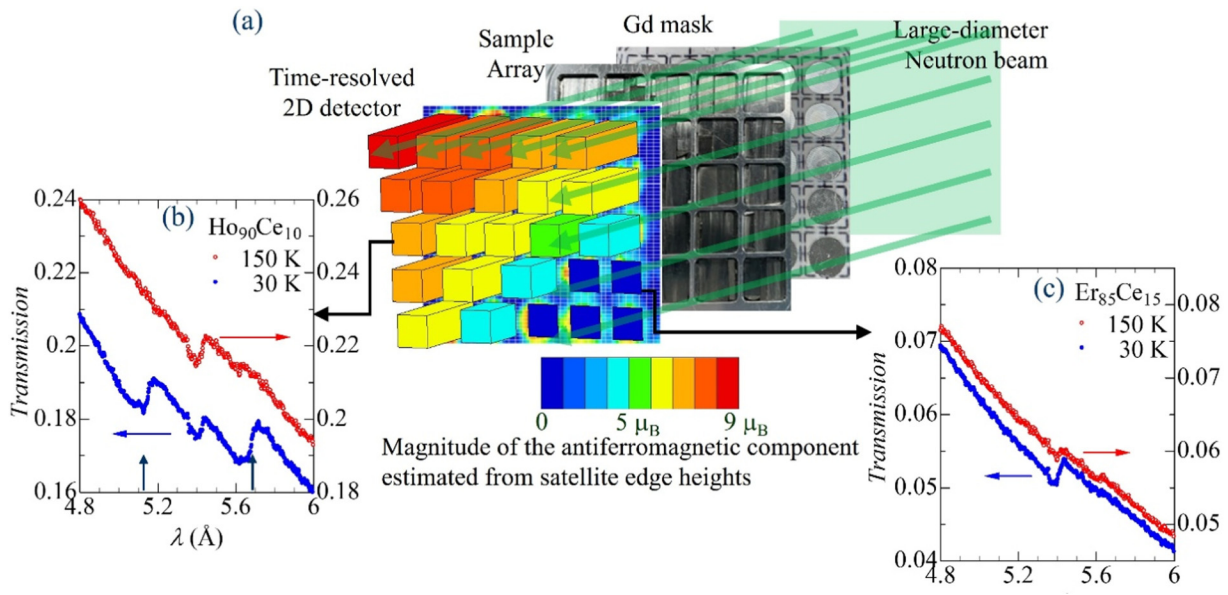

FIG. 3. Principle and typical results of multi-sample neutron transmission spectroscopy for polycrystalline samples with appropriate thicknesses (data were retrieved from Ref. 24). (a) Schematic illustrating the experimental setup and representative results for unpolarized neutrons and (b) and (c) examples of typical spectra.

samples simultaneously. Moreover, it effectively extracted magnetic structural information from these spectra. For example, the analysis of the heights of the satellite Bragg edges, marked by arrows in the figure, revealed variations in the magnitude of the magnetic moments organized into a helical structure. In this paper, we shall explore the advantages and challenges of simultaneous multi-sample measurements, drawing on the referenced success.[24]

Considering the capabilities of multi-sample transmission spectroscopy, it is crucial to assess the number of samples that can be measured simultaneously. Theoretically, the array size can be unlimited if only transmitted neutrons are captured by the detector array. However, one must be cautious about the potential of wide detectors to inadvertently capture diffracted neutrons. To reduce this risk, employing a chopper to filter out short-wavelength neutrons that cause forward scattering prior to their incidence is an effective strategy. For instance, setting a cutoff wavelength at 1/5 of the longest interplanar spacing would preclude diffraction at angles characterized by $2 \sin \theta < 1/5$. Therefore, if the detector array is positioned 300 mm behind the sample array ($l = 300$ mm), maintaining the sample array width (w) (equal to the detector array width) at 60 mm would effectively prevent contamination from diffraction lines. However, given the presence of certain magnetic structures with exceptionally long periods, a meticulous evaluation is necessary when configuring the actual experimental setup.

Subsequently, it is essential to investigate the lower limit of the individual sample size. The most significant factor in this context is the signal-to-noise (S/N) ratio of the spectrum, which is inherently dependent on the experimental objectives and the intensity of the incident beam at the utilized facility. As a result, it is challenging to establish definitive values for the sample size. However, the successful analysis using 6 mm diameter polycrystalline samples at J-PARC (0.7 MW)[24] serves as a practical benchmark for polycrystalline magnetic materials with large magnetic moments, providing valuable guidelines for future applications. Conversely, for single-crystal samples, as illustrated in Fig. 1, a sufficient signal has been obtained from a relatively small specimen (with dimensions of 1 mm). However, densely packing and aligning numerous small samples presents challenges. The angular dispersion $\Delta\varphi$ of the incident neutrons significantly impacts the parallelism of the neutron beam's path. For example, neutrons passing through an aperture of diameter d_a and traveling a distance L_0 to the sample will exhibit an angular spread defined by $\sin \Delta\varphi = d_a/L$. This dispersion causes a broadening of $l \sin \Delta\varphi = l\, d_a/L$ in a detector located at a distance l behind the sample. To avoid overlap of transmitted neutrons from adjacent samples, it is necessary to maintain a gap equivalent to $l\, d_a/L$ between the samples. If $\Delta\varphi$ equals 0.3° ($d_a/L = 1/180$), this corresponds to a width of approximately 2 mm when l is 300 mm. Reducing this value by placing the detector closer to the sample can lead to interference from diffracted neutrons, as previously discussed. Therefore, selecting conditions that meet the experimental objectives is crucial. For example, given the parameters mentioned ($w = 60$ mm and the gap between the samples = 2 mm), it is theoretically feasible to simultaneously measure up to 400 single-crystal samples, each measuring 1×1 mm^2, under these experimental conditions. When utilizing polycrystalline samples measuring 6×6 mm^2, it is feasible to measure up to 49 samples simultaneously. The capacity to measure 49 or 400 at the same time is considered sufficient for the optimization of material composition and processing. Therefore,

multi-sample spectroscopy is expected to be useful when a large number of samples need to be measured, especially when an automatic sample changer is not available in special environments.

Before concluding this section, it is crucial to address the significant limitations inherent to multi-sample transmission spectroscopy. A primary constraint is the necessity to conduct measurements under uniformly identical conditions for all samples simultaneously. In conventional neutron diffractometry, which focuses on individual samples, it is possible to precisely adjust the measurement temperature to suit the unique characteristic temperature of each sample and extend the measurement duration as needed to ensure experimental accuracy. On the other hand, such flexibility in adjusting experimental conditions is challenging when measuring multiple samples concurrently. In other words, conventional diffractometry is more suited for detailed investigations. It is important to note that the field of magnetic materials is currently experiencing a shift towards data-driven optimization, a trend that is promising but still in its nascent stages. However, for data-driven material optimization, precise physical details as features are not always necessary. Given these considerations, the high-throughput capabilities of multi-sample transmission spectroscopy hold significant promise.

2. Spectroscopic imaging

As highlighted in the Introduction, during the final implementation stage, a comprehensive evaluation of magnetic materials following assembly or operational use is desirable. This necessity arises because magnetic energies are much smaller than chemical bond energies of several electron volts (eV). For instance, the Zeeman energy of a magnetic moment of $10\,\mu_B$ in a 1 T magnetic field is less than 1 meV. Consequently, the magnetic state of materials is highly susceptible to subtle changes in the local environment, such as magnetic anisotropy during formation and minor variations in heat and stress during operation. This sensitivity extends to strain and magnetic poles on the surface, highlighting the need for methodologies that can nondestructively observe the microstructural and magnetic states within a material's interior.

Neutrons, recognized for their high penetration depth, have been conventionally used in this type of nondestructive analysis, known as neutron radiography.[25] The internal structures of objects have been imaged by exploiting the differences in neutron attenuation cross sections of various materials. Figure 4(b) shows the distribution of the ratio of the effective thickness, t_{eff}, derived from the neutron transmission measured in the 5–6 Å wavelength range, to the actual thickness, t_{actual}, for a non-oriented electromagnetic steel core with t_{actual} of 6 mm along the transmission direction, as shown in Fig. 4(a). In this image, the effective thickness, which correlates with the bulk density, appears relatively greater outside the curved section. The insights obtained from neutron attenuation imaging are instrumental for evaluating processing methods. However, this conventional technique does not allow for the visualization of the dispersion of magnetic anisotropy, which influences the magnetic properties or affects the flow of magnetic flux.

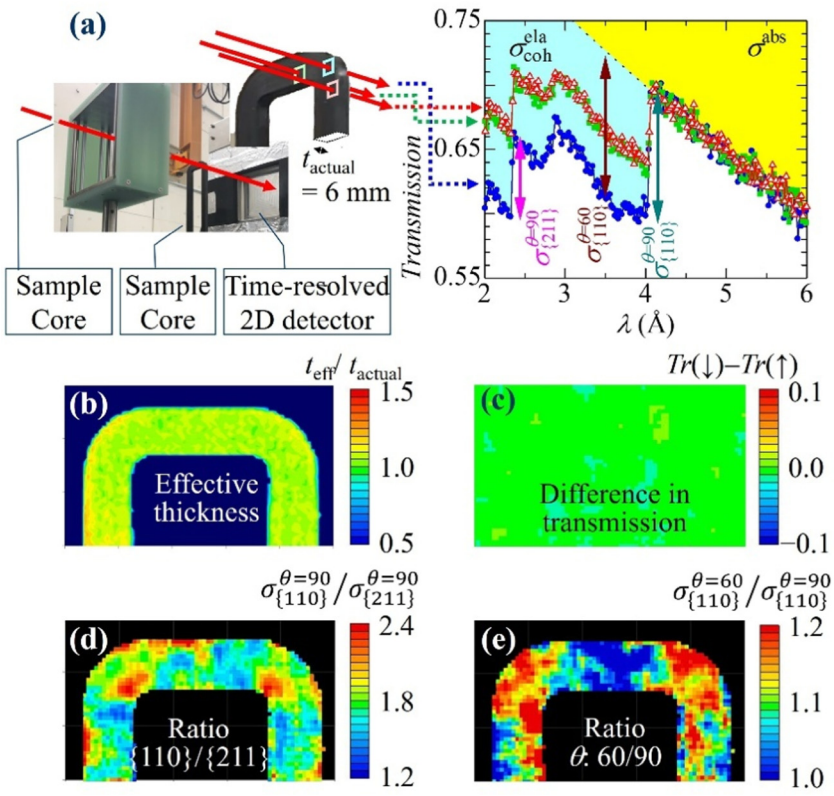

FIG. 4. Principle of Bragg edge imaging and typical results. (a) Experimental setup and transmission spectra from different regions of a non-oriented electrical steel wound core. The light blue and yellow areas in the spectra represent contributions from Bragg diffraction and absorption, respectively, for incident neutrons. (b) Distribution of the ratio of the effective thickness, t_{eff}, derived from the neutron transmission measured for unpolarized neutrons in the 5–6 Å wavelength range, to the actual thickness, t_{actual}, for a non-oriented electromagnetic steel core with t_{actual} of 6 mm along the transmission direction. (c) Differences in transmission between upward and downward polarized neutrons. (d) Maps showing the height ratio of the {110} to {211} edges for unpolarized neutrons. (e) Ratio maps comparing the contributions of {110} backscattering ($\theta = \pi/2$) with oblique diffraction ($\theta = \pi/3$) for unpolarized neutrons.

Conversely, as discussed in Sec. II, Bragg edges manifest in the wavelength region below a specific threshold (4.04 Å for iron). As in the multi-sample spectroscopy described above, the distribution of crystal structures can be visualized by analyzing the Bragg edges at different positions. This method has been utilized to analyze the internal microstructure of valuable cultural heritage items and artifacts without inflicting damage, thereby aiding in the determination of their archaeological origins.[10] More recently, such neutron imaging technique has been extended[26] to practical magnetic materials,[11,20,27] as well as other types of neutron imaging techniques, such as analysis of Larmor precession in magnetic flux,[28] differential neutron phase contrast,[29] and mapping of the depolarization coefficient.[30] In the case of the non-oriented iron core presented here, the shapes of the edges vary depending on their location, as depicted in Fig. 4(a). Figure 4(d) highlights these variations by focusing on the ratios of the heights of the {110} to {211} edges. The edge heights in the neutron transmission spectra are proportional to the diffraction intensity of the backscattered neutrons, and the intensity ratio of the {110} to {211} edges should be approximately 3 for random orientations when considering multiplicity factors, interplanar spacing, and minor differences in magnetic scattering. Consequently, the ⟨211⟩ axis appears relatively aligned with the incident neutron direction across the entire core, although this alignment diminishes on the inner side of the curved section. Conversely, Fig. 4(e) contrasts the contribution of {110} backscattering diffraction at the edge [$4.04\ \text{Å} = 2d_{110}\sin(\pi/2)$] with that of oblique diffraction observed at a shorter wavelength [$3.5\ \text{Å} = 2d_{110}\sin(\pi/3)$]. Given that this ratio approximates 0.75 for random orientations, the ⟨110⟩ axis exhibits a tilt relative to the incident direction, with this inclination intensifying within the curved sections. These observations suggest that, after stress-relief annealing above recrystallization temperature,[31] the forming process continues to influence the crystal structure. Therefore, by analyzing the features of the transmission spectrum of neutrons, a preliminary visualization of crystal texture information is achievable.

For a more detailed examination of this crystal texture, it is necessary to apply methods such as Rietveld refinement to the collected spectra. However, as discussed above, the transmission spectroscopy technique is less sensitive than diffractometry for detecting weak reflections required for such analyses. At this stage, it is crucial to recognize that the precise data demanded in fundamental science may not always be necessary for enhancing manufacturing processes. In practical scenarios, where the focus is on improving processing or assembly procedures and preventing degradation during use, it is often sufficient to correlate descriptors related to microstructural changes and magnetic properties through machine learning from numerous examples. In such contexts, the straightforward spectral mapping demonstrated here can be effectively utilized. Let us now consider the imaging of magnetic structures, a critical factor influencing magnetic properties. As we have observed, the treatment of magnetic scattering varies significantly between antiferromagnets and ferromagnets; in antiferromagnets, magnetic scattering occurs at different wavelengths from nuclear scattering, whereas in ferromagnets, these scatterings always overlap. While we have previously discussed multi-sample transmission spectroscopy for antiferromagnets, our focus here will be on ferromagnets. The use of polarized neutrons is particularly valuable for imaging these materials.

Let us consider how the flow of magnetic flux, the arrangement of magnetic domains across micrometer-to-millimeter-scale grains, and magnetic structures within nanometer-scale composites manifest when examined with polarized neutrons. Equations (4a) and (4b) demonstrates that when neutrons polarized along the Z direction are incident from the X direction, the polarization dependence of the backscattering intensity in a microcrystal correlates with the Z component of the magnetization direction. By analogy with the derivation of Eq. (3), the height of the Bragg edge similarly correlates with the Z component of the magnetization direction. Although transmission spectroscopy provides information averaged over the thickness of the sample, its unique capability enables the visualization of the internal magnetization states of bulk devices—a detail that is typically unattainable using alternative methods. For instance, in a transformer equipped with a manganese zinc ferrite core wrapped in copper windings, when fully saturated, Bragg-edge spectroscopic imaging recently revealed that the magnetization vector rotates along the circumferential direction of the toroidal core.[20] While this behavior aligns with expectations from Ampère's law, it had previously been inferred only indirectly through integrated values of magnetic flux captured by the electromotive force induced in an external pick-up coil. This example clearly demonstrates that the deep penetration capability of neutrons enables the direct observation of internal magnetization states that were previously unobservable. Meanwhile, under what circumstances can such imaging be performed? In this study, we further investigate the versatility of this method.

While it is possible to visualize the internal magnetic states of devices in a saturated state as shown previously,[20] it is important to recognize that magnetic cores do not operate in the fully saturated regions. In practical magnetic materials, as the magnetic field increases, magnetization initially rises easily due to the movement of magnetic domain walls and then gradually approaches saturation as the magnetization vector rotates away from the magnetic easy axis. Typically, this process is inferred from observations made at the surface of the device. However, can the changes in the internal magnetization state at each location be directly observed during these processes?

Figure 4(c) depicts the differences in the transmission of upward and downward polarized neutron beams when a closed magnetic circuit was formed by integrating a neodymium magnet ($\mu_0 M_s = 1.2$ T) into the core of the non-oriented electrical steel sheet discussed previously. In this illustration, no difference in transmission is apparent. For non-oriented electrical steel sheets, the transition from magnetic wall movement to magnetization rotation is believed to occur around 1.6 T.[32] Therefore, at 1.2 T, the magnetization within each grain is likely still tilted from the average magnetization direction toward the magnetic easy axis. In such cases, the neutron spin undergoes Larmor precession around the tilted magnetic flux lines that are different for each grain. During this precession, depolarization occurs, which can be described as follows:[33]

$$P = P_0\left[1 - \frac{1}{2}\left(\frac{\Upsilon_n m_n}{h}\delta B_t \lambda\right)^2\right]^{\frac{D}{\delta}}, \tag{5}$$

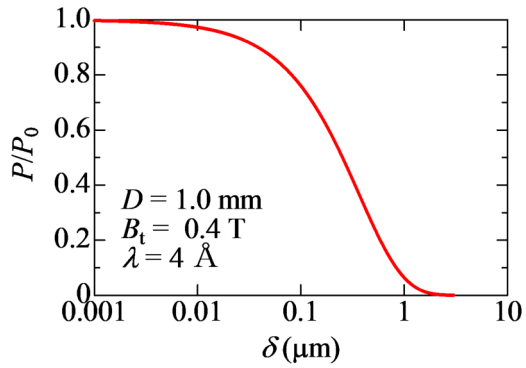

FIG. 5. Depolarization due to various scales of inhomogeneity. Variation in the polarization of neutrons at a wavelength of 4 Å and a depth of 1 mm, characterized by a typical heterogeneity size δ and a transverse magnetic field dispersion B_t of 0.4 T.

where P and P_0 are the polarizations of the neutrons and their initial values, respectively; γ_n denotes the gyromagnetic ratio; m_n denotes the neutron mass; h is Planck's constant; δ is the average domain size; D is the penetration depth; and B_t is the transverse magnetic field dispersion. Figure 5 depicts the change in polarization at a depth of 1 mm when $B_t = 0.4$ T. From this figure, it is evident that in non-oriented electrical steel, which features magnetic domains on the scale of tens of micrometers,[34] maintaining neutron polarization during deep penetration is challenging unless the material is fully saturated.

This observation suggests that transmission spectroscopy may not be ideal for evaluating conventional ferromagnetic materials. However, Fig. 5 depicts that depolarization does not occur when the scale of magnetization inhomogeneity is sufficiently small. Therefore, transmission spectroscopy can prove valuable for assessing nanocomposite magnetic materials, which have recently emerged as promising next-generation materials. These materials, such as exchange spring magnets,[35,36] exhibit magnetic states that vary with operating conditions, including the magnetization directions of the two nanophases. Evaluating these states in bulk components using existing technologies is particularly challenging. The magnetic coupling and interfacial magnetic anisotropy between the nanocomposite phases are likely sensitive to fabrication conditions and degradation, posing significant challenges for the integration of such novel materials into devices. Neutron transmission spectroscopy allows for the analysis of multiphase materials by differentiating phases with distinct crystalline structures, as each phase's Bragg edge appears at different wavelengths. Furthermore, as illustrated in Fig. 5, the polarization of neutrons at each edge is not disturbed by magnetic inhomogeneities on the nanoscale, enabling expectations of mapping magnetization orientation for each phase. In other words, leveraging the capabilities of transmission spectroscopy may facilitate the simultaneous mapping of nanoscale magnetic states and nanocrystalline textures in multiphase nanocomposites during post-production, integration, and operational stages.

IV. SUMMARY AND PROSPECTIVE

This study investigated the applicability of Bragg-edge transmission spectroscopy for analyzing complex magnetic structures in advanced magnetic materials. The incorporation of multi-sample transmission measurements significantly increased experimental throughput, enabling the generation of large datasets essential for materials optimization. The non-destructive nature of the method allowed for internal magnetic structure visualization under both manufacturing and operational conditions. These capabilities can improve quality control and functional evaluation in technologies reliant on magnetic materials, including those used in energy and data storage. Furthermore, we can expect that this approach enables microstructural and magnetic state mapping in multiphase nanocomposite systems, supporting assessment after fabrication, during integration, and in-service operation. While polarized neutron Bragg-edge analysis showed limitations in resolving micrometer-scale domains in conventional ferromagnetic devices, it showed significant potential for characterizing future nanostructured magnetic materials with complex internal order.

Before concluding this paper, we would like to briefly refer the potential of transmission spectroscopy to make neutron diffraction more accessible. In the field of x-ray diffraction, alongside large-scale synchrotron facilities, small-scale laboratory x-ray diffraction instruments (lab-XRD) are commonly installed in universities and companies, providing ample opportunities for the rapid testing of new ideas. In contrast, lab-scale neutron diffraction instruments are rarely available, and this lack is frequently cited as the critical barrier to the utilization of neutrons in magnetic materials development.[37,38] It is worth considering whether the distinct characteristics of neutron transmission spectroscopy could help to address this challenge.

First, it should be noted that even with future advancements in small neutron source technology, the number of neutrons that can be generated in a laboratory setting will remain significantly lower than that available at large-scale neutron facilities. When using such low-intensity sources, focusing optics becomes crucial to deliver the required neutron flux to the sample. However, as depicted in Fig. 6(a), in diffractometry, the convergence angle Δφ of the incident beam significantly affects the resolution of the diffraction angle. For instance, achieving a resolution of 0.1° necessitates that the convergence angle not exceed 0.1°. Without the ability to focus, one alternative would be to increase the sample size to enhance the total

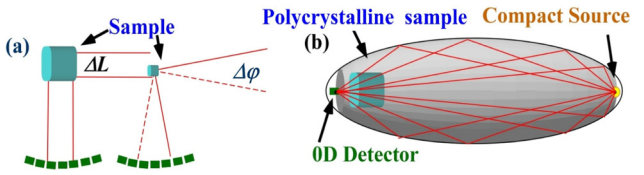

FIG. 6. Focusing optics and the sample size in neutron diffractometry and spectroscopy. (a) Diagram depicting the resolution of a focused neutron beam across a range of incident angle sizes (Δθ) striking a sample of size (ΔL) and (b) illustration of a spectrometer using a pulsed neutron generator with a time-resolved detector located at the foci of a rotating elliptical neutron mirror.

incidence. However, in this scenario, as the neutron path length varies with the sample size, it results in degraded time-of-flight (ToF) resolution, thereby reducing the wavelength resolution. For this reason, it is not easy to perform effective diffraction measurements using low-intensity neutron sources.

In the transmission spectroscopy of polycrystalline materials, the positions of Bragg edges in the spectra are independent of the angle of the incident beam, with the resolution being solely determined by the flight distance from the source to the detector and the pulse width. A theoretical setup involves placing a point neutron source and a zero-dimensional time-resolutive detector at the focal points of a rotating elliptical neutron mirror. This configuration ensures constant flight distances, irrespective of the sample's position, size, or the angle of the incident beam, as depicted in Fig. 6(b). In theory, this arrangement allows for the measurement of Bragg edges by exposing all of the generated neutrons to a large sample volume. In practice, current neutron mirrors are limited to reflections of up to approximately 3°;[39] nevertheless, under such conditions, the collected neutron flux is 1000 times greater than that at 0.1°. Although this concept remains theoretical at present, it may nonetheless merit further exploration.

ACKNOWLEDGMENTS

Experiments at BL22 of J-PARC were performed using user programs (Grant Nos. 2017A0042, 2018A0062, and 2021B0189). A part of this work was supported by "Advanced Research Infrastructure for Materials and Nanotechnology in Japan (ARIM)" of the Ministry of Education, Culture, Sports, Science and Technology (MEXT) (Grant No. 24NM5119). This work was partially supported by JSPS KAKENHI (Grant No. 19H04400); MEXT-Program for Creation of Innovative Core Technology for Power Electronics (Grant No. JPJ009777); and JST-Mirai Program, Japan (Grant No. JPMJMI18A3). During the preparation of this work, the author used the NIMS Azure Chat to refine English. After using this tool or service, the author(s) reviewed and edited the content as needed and took (s) full responsibility for the content of the publication.

AUTHOR DECLARATIONS

Conflict of interest statement

The authors have no conflicts to disclose.

Author Contributions

Hiroaki Mamiya: Conceptualization (equal); Data curation (equal); Methodology (equal); Writing – original draft (equal); Writing – review & editing (equal). **Noriki Terada:** Conceptualization (equal); Methodology (equal); Writing – original draft (equal); Writing – review & editing (equal). **Kosuke Hiroi:** Conceptualization (equal); Data curation (equal); Writing – review & editing (equal). **Takenao Shinohara:** Conceptualization (equal); Data curation (equal); Writing – review & editing (equal). **Hossein Sepehri-Amin:** Conceptualization (equal); Methodology (equal); Writing – review & editing (equal).

DATA AVAILABILITY

The data that support the findings of this study are available from the corresponding author upon reasonable request.

REFERENCES

[1]Survey using Scopus, Elsevier B.V. (2025). See https://www.scopus.com/.
[2]S. Funahashi, S. Katano, and R. A. Robinson, Phys. B: Condens. Matter **213–214**, 1–1052 (1995), available at https://www.sciencedirect.com/journal/physica-b-condensed-matter/vol/213/suppl/C.
[3]Y. Ohtani, H. Hatakeyama, H. Nakagome, T. Usami, T. Okamura, and S. Kabashima, Cryocoolers **10**, 581 (1999).
[4]H. Iwasaki, A. T. Saito, A. Tsutai, and M. Sahashi, IEEE Trans. Magn. **33**, 2875 (1997).
[5]S. Iwasaki and K. Ouchi, IEEE Trans. Magn. **14**, 849 (1978).
[6]R. Coehoorn, D. B. Demooij, J. P. W. B. Duchateau, and K. H. J. Buschow, J. Phys **49**, 669 (1988).
[7]S. Kasai, M. Namikawa, and T. Hiratani, JFE Tech. Rep. **21**, 14 (2016).
[8]S. Dall'Olio *et al.*, Int. J. Refrig. **132**, 243 (2021).
[9]F. Salvemini, V. Luzin, M. Avdeev, A. Tremsin, A. Sokolova, A. Gregg, C. Wensrich, S. Gatenby, M. J. Kim, and F. Grazzi, Mater. Sci. Forum **983**, 15 (2020).
[10]Y. Su, K. Oikawa, T. Shinohara, T. Kai, T. Horino, O. Idohara, Y. Misaka, and Y. Tomota, Sci. Rep. **11**, 4155 (2021).
[11]H. Mamiya, Y. Oba, N. Terada, K. Hiroi, and T. Shinohara, IEEE Trans. Magn. **59**, 6500505 (2023).
[12]T. Shinohara, T. Kai, K. Oikawa, T. Nakatani, M. Segawa, K. Hiroi, Y. Su, M. Ooi, M. Harada, H. Iikura, H. Hayashida, J. D. Parker, Y. Matsumoto, T. Kamiyama, H. Sato, and Y. Kiyanagi, Rev. Sci. Instrum. **91**, 043302 (2020).
[13]J. D. Parker, M. Harada, H. Hayashida, K. Hiroi, T. Kai, Y. Matsumoto, T. Nakatani, K. Oikawa, M. Segawa, T. Shinohara, Y. Su, A. Takada, T. Tanimori, and Y. Kiyanagi, Mater. Res. Proc. **15**, 102 (2020).
[14]G. L. Squires, *Introduction to the Theory of Thermal Neutron Scattering* (Cambridge University Press, New York, 2012).
[15]E. Fermi, W. J. Sturm, and R. G. Sachs, Phys. Rev. **71**, 589 (1947).
[16]W. Kockelmann, G. Frei, E. H. Lehmann, P. Vontobel, and J. R. Santisteban, Nucl. Instrum. Methods Phys. Res. Sec. A **578**, 421 (2007).
[17]H. Mamiya, Y. Oba, N. Terada, N. Watanabe, K. Hiroi, T. Shinohara, and K. Oikawa, Sci. Rep. **7**, 15516 (2017).
[18]B. L. Rhodes, S. Legvold, and F. H. Spedding, Phys. Rev. **109**, 1547 (1958).
[19]H. Sato, T. Kamiyama, and Y. Kiyanagi, Mater. Trans. **52**, 1294 (2011).
[20]H. Mamiya, Y. Oba, N. Terada, K. Hiroi, T. Ohkubo, and T. Shinohara, Sci. Rep. **13**, 9184 (2023).
[21]J. E. Rix, J. K. R. Weber, L. J. Santodonato, B. Hill, L. M. Walker, R. McPherson, J. Wenzel, S. E. Hammons, J. Hodges, M. Rennich, and K. J. Volin, Rev. Sci. Instrum. **78**, 013907 (2007).
[22]D. Vong, E. C. Novak, M. M. Ruiz-Rodriguez, S. R. Elorfi, B. Thomas, A. J. Morris, A. J. Moulé, and L. L. Daemen, Rev. Sci. Instrum. **94**, 085108 (2023).
[23]M. Dou, H. Hu, Z. Huang, B. Yuan, Q. Lin, W. Luo, F. Ye, H. Cheng, H. Jiang, Y. Ke, H. Cheng, B. Bai, and X. Tong, Cryogenics **141**, 103881 (2024).
[24]H. Mamiya, N. Terada, S. R. Larsen, N. Tsujii, K. Hiroi, T. Shinohara, and H. Sepehri-Amin, Phys. Rev. Res. **7**, 013233 (2025).
[25]M. R. Hawkesworth and J. Walker, J. Mater. Sci. **4**, 817 (1969).
[26]N. Kardjilov, I. Manke, R. Woracek, A. Hilger, and J. Banhart, "Advances in neutron imaging," Mater. Today **21**, 652–672 (2018).
[27]S. Sasada, Y. Takahashi, K. Takeuchi, K. Hiroi, Y. H. Su, T. Shinohara, K. Watanabe, and A. Uritani, Jpn. J. Appl. Phys. **61**, 046004 (2022).
[28]K. Hiroi, T. Shinohara, H. Hayashida, J. D. Parker, Y. H. Su, K. Oikawa, T. Kai, and Y. Kiyanagi, Phys. B **551**, 146 (2018).
[29]M. Strobl, W. Treimer, P. Walter, S. Keil, and I. Manke, Appl. Phys. Lett. **91**, 254104 (2007).

[30]M. Busi, E. Polatidis, C. Sofras, P. Boillat, A. Ruffo, C. Leinenbach, and M. Strobl, Mater. Today Adv. **16**, 100302 (2022).
[31]R. Karami, D. Butler, and S. Tamimi, Int. J. Adv. Manuf. Technol. **133**, 1083–1109 (2024).
[32]H. G. Kang, K. M. Lee, M. Y. Huh, J. S. Kim, J. T. Park, and O. Engler, J. Magn. Magn. Mater. **323**, 2248 (2011).
[33]S. Mitsuda and Y. Endoh, J. Phys. Soc. Jpn. **54**, 1570 (1985).
[34]M. Gallaugher, N. Brodusch, R. Gauvin, and R. R. Chromik, Ultramicroscopy **142**, 40 (2014).
[35]R. Coehoorn, D.-B. de Mooij, and C. de Waard, J. Magn. Magn. Mater. **80**, 101 (1989).
[36]H. Martínez-Sánchez, L. Marín, F. Machuca-Martínez, and L. A. Rodríguez, Heliyon **10**, e32358 (2024).
[37]T. Brückel *et al.*, Neutron News **31**, 24 (2020).
[38]See https://www.ucans.org/index.html for "Union for Compact Accelerator-driven Neutron Sources."
[39]C. Schanzer, M. Schneider, and P. Böni, J. Phys.: Conf. Ser. **746**, 012024 (2016).